2020

Putting Photomechanical Switches to Work: An *Ab Initio* Multiple Spawning Study of Donor-Accepted Stenhouse Adducts

D. M. Martinez
Stanford University

U. Raucci
Stanford University

K. N. Ferreras
Stanford University

Todd J. Martínez
Stanford University

Martinez, D. M.; Raucci, U.; Ferreras, K. N.; and Martínez, Todd J., "Putting Photomechanical Switches to Work: An *Ab Initio* Multiple Spawning Study of Donor-Accepted Stenhouse Adducts" (2020). *The Journal of Physical Chemistry Letters*. 26.
https://doi.org/10.1021/acs.jpclett.0c02401

Putting Photomechanical Switches to Work: An Ab Initio Multiple Spawning Study of Donor Acceptor Stenhouse Adducts

D. M. Sanchez,[1,2] U. Raucci,[1,2] K. N. Ferreras,[1,2] and Todd J. Martínez[1,2,*]

[1]*SLAC National Accelerator Laboratory, Menlo Park, USA.*
[2]*Department of Chemistry and The PULSE Institute, Stanford University, Stanford, USA.*

Abstract: Photomechanical switches are light sensitive molecules capable of transducing the energy of a photon into mechanical work via photodynamics. In this letter, we present the first atomistic investigation of the photodynamics of a novel class of photochromes called Donor-Accepter Stenhouse Adducts (DASA) using state-of-the-art *ab-initio* Multiple Spawning interfaced with State-Averaged Complete Active Space Self-Consistent Field Theory. Understanding the **Z**/**E** photoisomerization mechanism in DASAs at the molecular level is crucial in designing new derivatives with improved photo-switching capabilities. Our dynamics simulations show that the actinic step is comprised of competing nonradiative relaxation pathways that collectively contribute to DASAs' low (21% in Toluene) photoisomerization quantum yield. Furthermore, we highlight the important role the intramolecular hydrogen bond plays in the selectivity of photoisomerization in DASAs, identifying it as a possible structural element to tune DASA properties. Our fully *ab initio* simulations reveal the key degrees of freedom involved in the actinic step, paving the way for the rational design of new generations of DASAs with improved quantum yield and efficiency.

Keywords: Photoisomerization, Nonadiabatic Dynamics, Excited State Proton Transfer, Ab Initio Multiple Spawning

* Corresponding author. Email: toddjmartinez@gmail.com

Table of Contents Figure

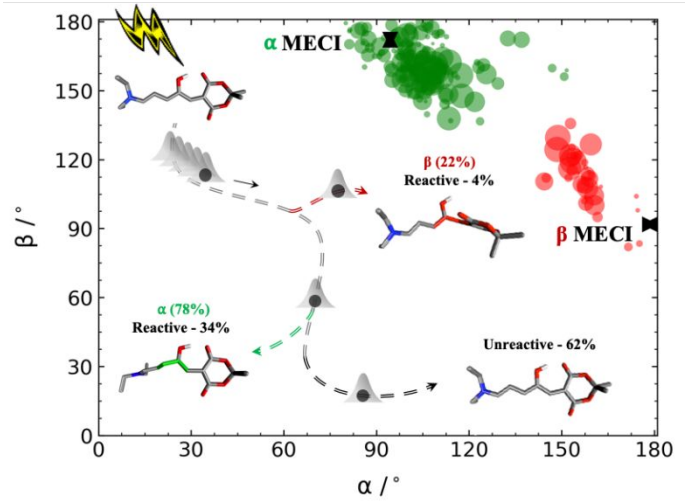

Extracting mechanical work from photoinduced processes has proven to be a difficult task involving combined efforts between different subfields of chemistry, physics, and engineering. In recent years, the focus of the photomechanical community has been to design unique families of photo-switches, responsible for converting incident light in the ultraviolet (UV) region into mechanical work via large macroscopic shape changes.[1-7] These macroscale deformations of materials start at the molecular level on the picosecond or faster timescales with the absorption of incident light in the ultraviolet or visible (UV-Vis) region. Several families of photo-switches capable of undergoing such processes have been proposed in literature,[8-11] but all suffer from some form of photo/thermal instability, issues regarding polarity, solubility, or suboptimal excited-state features (i.e. absorption wavelength, lifetime, quantum yield). For example, spiropyran and diarylethene derivatives have shown small fatigue resistance and photostability,[12-13] while supramolecular assemblies containing azobenzenes switch between two colored states resulting in limited light penetration into materials.

Recently, a new class of photochromes named Donor-Acceptor Stenhouse Adducts (DASAs) have been synthesized and characterized by Read de Alaniz and co-workers.[14-17] As shown in Figure 1a, these novel chromophores consist of a donor and acceptor group linked together via a hydroxylated triene bridge. DASAs have shown potential as powerful photo-switches due to large structural changes resulting in greater than 50% total volume contraction,[14] negative solvatochromism from a colored reactant to a colorless product (increasing light penetration and conversion yield), and tunable absorption profiles that depend directly on the donor and acceptor groups. To improve upon these properties, several DASA "generations" were synthesized where the R groups in the amine donor and the Meldrum's acid acceptor were

replaced with aromatic rings[16] (2nd generation) or conjugated heteroatoms[17] (3rd generation), respectively.

In addition to spectroscopic properties, DASAs have received considerable attention due to their two-part mechanism involving a fast actinic step and a slow thermal step.[18-22] Using time-resolved UV-Vis absorption and infrared (IR) spectroscopy experiments, Feringa and coworkers have proposed that **1** is promoted to an excited electronic state where it relaxes back to the ground state via a **Z**/**E** photoisomerization nonradiative relaxation channel on the ps timescale.[20] The timescale for **Z**/**E** photoisomerization is greatly influenced by the donor and acceptor groups: converting Meldrum's acid to barbituric acid resulted in a doubling of the excited state lifetime.[20] Furthermore, a relatively low quantum yield of 21% or less was observed for the EEEZ (**3** in Figure 1b) photoproduct of 1st and 2nd generation DASAs in a range of solvents with varying polarity. Once on the ground state, DASA undergoes a thermal 4π-electrocyclization leading to the *anti* ring-closed cyclopentenone form (**5** in Figure 1b).[18,22-23] Intermediates along the ring-closing reaction coordinate were identified in solvent via direct comparison between measured and calculated transient IR.[20,22] In addition, an alternative thermal pathway was proposed with the identification of an EZZZ intermediate that leads to a *syn* ring-closed cyclopentenone product (**6** in Figure 1b).[22] However, this *syn* adduct has yet to be observed in experiment. Lastly, the actinic step is relatively unaffected by solvent and concentration effects,[22,24] while it is not fully understood to what degree solvent, and the environment as a whole, influence the thermal 4π-electrocyclization.

So far, there have been few computational studies aimed at characterizing key excited state features[25-26] and describing the **Z**/**E** photoisomerization and 4π-electrocyclization in DASAs.[21-22,27] Using Time-Dependent Density Functional Theory (TD-DFT) and State-Average

Complete Active-Space Self-Consistent Field Theory (SA-CASSCF), García-Iriepa and coworkers identified critical points (e.g. S_1/S_0 minimum conical intersection (MECI) and S_1 minima) along the **Z**/**E** photoisomerization coordinate on the S_1 adiabatic state.[27] In addition, Zulfikri and coworkers explored the ground-state ring-closing mechanism by computing energy barriers between all involved intermediates leading to **5** and **6**.[22] However, several questions regarding the molecular response of DASAs to photoexcitation are still open.[28] For example, the possibility of DASA to photoisomerize across alternate bonds along the triene bridge (which we label as α, β, and γ as shown in Figure 1b), the influence of the donor and the acceptor group on timescale and quantum yield, and the role of the solvent in the switching process. A fuller understanding of the detailed photodynamics of DASAs will enable rational design of improved DASA photoswitches.

In this letter, we use GPU-accelerated SA-CASSCF[29-31] in TeraChem[32-34] interfaced with *ab-initio* Multiple Spawning (AIMS)[35-38] to elucidate the photodynamics of Meldrum's acid 1st generation DASA in the gas-phase. Our simulations show competing nonradiative relaxation channels present in the actinic step, previously overlooked by MEP studies.[27] The alternate relaxation channels arise because of the presence of several conical intersections (CI) corresponding to isomerization about different C-C torsional angles on the hexatriene bridge. Similar behavior has been observed in large conjugated polyene systems such as retinal protonated Schiff base.[39-41] These competing pathways contribute to the low cyclization quantum yield observed in DASAs, which have been measured in Toluene to be 21.0%, 10.6%, and 14.5% for 1st generation (Meldrum's and barbituric acid) and 2nd generation DASAs, respectively.[20] Indeed, isomerization around the β bond accesses unproductive ground-state

intermediates, effectively shutting off the 4π-electrocyclization, while isomerization around γ results in reforming the ring-open photoreactant **1**.

We performed *ab-initio* nonadiabatic molecular dynamics with AIMS using an active space consisting of two electrons in two π orbitals determined to minimize the 3 lowest singlet electronic states in conjunction with the 6-31G** basis set, hereafter referred to as SA3-CAS(2,2)SCF/6-31G**. The chosen active space agreed well with previous large active-space calculations[27] and was benchmarked against single-point energy calculations at the 3-state Extended Multistate Second Order Perturbation Theory (SA3-XMS-CAS(2,2)PT2/6-31G**) level of theory[42-43] along the α and β photoisomerization pathways (Figures S1 and S2). In the Franck Condon (FC) region, the triene moiety is completely planar allowing a complete π-conjugation along its skeleton. The electronic excitation to the S_1 excited state is bright and corresponds to a π-π* one-electron excitation, which is localized on the π-conjugated skeleton of the triene backbone (see Figure S3). Upon excitation to S_1, the wavepacket moves towards a local minimum along a bond-length alternation (BLA) coordinate where it maintains a planar structure. The system can then evolve along different isomerization channels corresponding to the α and β dihedral angles on the triene bridge (Figure 1b). The S_1/S_0 MECIs show a common feature of a 90-degree twist along one of the isomerizable bonds.

The AIMS simulations were initiated from 50 initial conditions (positions and momenta) sampled from a 0K harmonic Wigner distribution corresponding to the PBE0[44]/6-31G** ground state minimum. Figure S4 compares the UV absorption spectrum computed from these initial conditions to the experimental spectrum, and the shapes of the two spectra are in good agreement. The time-evolution of the wavepacket population is followed on the S_0, S_1, and S_2 adiabats through the first 4ps of DASA photodynamics and reported in the lower panel of Figure

2a. The S_1 population trace was fit to a monoexponential function, $P(t) = A\exp\left(-t/\tau\right)$, where P(t) is the population at time t, τ is the decay constant in fs, and A is a fitting parameter. The computed decay constant is 1.8 +/- 0.2ps, which agrees fairly well with the reported experimental lifetimes of 2.7ps and 2.1ps in Toluene and Dichloromethane, respectively.[20] The shorter lifetime in the gas-phase could be due to the absence of steric and electrostatic effects from the solvent that may influence the isomerization dynamics. Upon photoexcitation to S_1, the wavepacket relaxes back to S_0 via two distinct S_0/S_1 CIs that pertain to twisting around the α or β dihedral angles. Partitioning each spawning event according to which of the α/β pathways it follows shows that both nonradiative relaxation channels occur on roughly the same timescale (upper panel of Figure 2a). Figure S5 shows that there is no obvious correlation between the decay channel selectivity or decay timescale and either the initial excitation energy or α/β pre-twisting.

The population transfer vs S_1/S_0 energy gap of all spawning geometries is plotted in the lower panel of Figure 2b, showing that the majority of the spawning events take place within 0.1eV of the intersection seam, with a few reaching as far as 0.4eV. Furthermore, as shown in Figure S7, TBFs transfer population in a region of the intersection seam shifted towards higher energy with respect to the MECI. It is important to note that this shift towards higher energy is partly attributed to the high internal energy of the TBFs caused by the sampling of ICs from a harmonic Wigner distribution. Overall, these observations are consistent with previous studies showing that due to the high dimensionality of the CI seam and nonequilibrium nature of excited-state dynamics, the molecule may never reach the exact nuclear configuration corresponding to the MECI and cross the intersection seam at a point that possess higher internal energy.[45-47]

In Figure 3, the S_1 to S_0 population transfer events are examined in more detail as a function of the α, β, and γ twisting angles. The α and β decay channels are completely orthogonal to one another (i.e. the molecule isomerizes around either α or β). This is evident in Figure 3a, which shows the clear partitioning of all spawning events into either α or β. Approximately, 78% of the wavepacket relaxes through the α pathway while only 22% passes through β. This is in agreement with the computed barriers for the α and β twisting (**Fig. S1**), which are 0.02 and 0.05 eV, respectively. The inclusion of dynamic electron correlation is expected to play a small role in the general accessibility of the α and β pathways, but it may slightly influence their computed branching ratio. The spawning geometries along with their respective MECIs for α and β are shown in the inset of Figure 3a. The α spawning geometries are distributed around the optimized α-MECI, while the β geometries are less well clustered around the optimized β–MECI. This is further examined in Figure 3b, which shows that twisting around β is highly coupled to twisting around the γ dihedral. The spawning geometries leading to the α decay are only slightly twisted along γ (γ < 30°). In contrast, γ is twisted by more than 40° during the β twisting. This concerted movement of β and γ angles helps to maintain the intramolecular hydrogen bond between the hydroxyl and the Meldrum's acid. Lastly, the **Z**/**E** photoisomerization follows a one-bond-flipping (OBF) mechanism for both α and β, which is shown by representative α and β AIMS TBFs in the movies of the supporting information.

The intramolecular hydrogen bond plays an important role in the isomerization selectivity in DASA photodynamics. Figure 4 reports the population transfer as function of the intramolecular hydrogen bond coordinate (δ_{PT}) for all spawning geometries. Negative values of δ_{PT} represent the transfer of the proton from the hydroxyl to the carbonyl group in the Meldrum's

acid. Approximately, 3% of the trajectory basis functions (TBFs) isomerizing through α experience proton transfer. The transfer of a proton along with the increase of negative charge on the hydroxyl oxygen work together to decrease the strength of the α isomerizing bond via the BLA of the hexatriene bridge. Hence, the hydrogen bond represents a key design element to change the photoisomerization selectivity: changing the intramolecular hydrogen bond strength should tune the branching ratio between α and β.

In Figure 5, we go beyond branching between the α and β pathways and report the branching ratio of the AIMS trajectories that led to "reactive" and "unreactive" α and β cis photoproducts. Here, reactive and unreactive pertains to those trajectories that did or did not form the cis photoproducts of α or β, respectively. All TBFs on S_1 are colored grey, while green (upper panel) and red (lower panel) lines represent TBFs evolving on S_0 toward the α (EEEZ) or β (EEZE) photoproducts from the photoreactant (EEZZ). All unreactive TBFs coming back to reform the photoreactant (EEZZ) on S_0 are colored black. The thickness of the line is proportional to the renormalized population at time t of a particular TBF during the AIMS dynamics. Approximately, 34% of the population formed the reactive α photoproduct, while only 4.0% formed the reactive β photoproduct. The final branching ratio is reported as 0.34: 0.04: 0.62 for EEEZ, EEZE and EEZZ, respectively. The small yield computed for the EEEZ conformer is in relatively good agreement with the experimental values of 0.21 and 0.11 measured in Toluene and dichloromethane, respectively.[20] The population transfer efficiency of the α channel is 44% (population $\alpha_{reactive}$/ population α_{TBFs}), which is approximately two-times that of β, showing that α is a much more efficient mode for nonradiative relaxation in DASAs. The low quantum yield for reactive α isomerization is related to the topology of the CI. Figure S6a shows the branching space at the α MECI geometry is sloped towards photoreactant, which

is in agreement with previous large active-space SA2-CAS(12,12)SCF calculations.[27] This drives the wavepacket towards photoreactant, as it is energetically unfavorable to go uphill to form the reactive α photoproduct. A sloped intersection is also observed for the β MECI (Figure S6b).

In conclusion, the photodynamics of the Meldrum's acid 1st generation DASA has been investigated for the first-time using AIMS, revealing a complex interplay of internal coordinates (α, β, γ and δ_{PT}) involved in its nonadiabatic transition from S_1 to S_0. Our simulations identify competing photoisomerization pathways (α, β, and γ) that follow OBF mechanisms to form a variety of ground-state structures. We show that the intramolecular hydrogen bond present in DASAs may play a key role in promoting the productive α photoisomerization pathway, effectively mitigating the coupled torsion around the β and γ dihedral angles. Lastly, our dynamics show that the low quantum yields for the α and β photoisomerization pathways in the actinic step are due to the sloped nature of the α/β S_0/S_1 branching spaces. Building upon this study, it is clear that the influence of solvation effects on the nonadiabatic dynamics will be fundamental. On one hand, electrostatic and steric effects can alter the topology of the CIs, leading to changes in observed branching ratios and lifetimes, while on the other hand, intermolecular hydrogen bonding in protic solvents can influence the selectivity between the α and β pathways. Changing the topology of the conical intersection towards a more peaked shape along with strengthening the intramolecular hydrogen bond represent the next steps towards designing new generations of DASAs with improved efficiency. Work in this direction is currently underway.

Acknowledgments

This work was supported by the MURI program of the Office of Naval Research (N00014-18-1-2624).

Supporting Information

Comparisons of CASSCF and MSPT2 energetics for critical points and reaction pathways, analysis of wavefunctions in terms of active space orbitals and configuration interaction coefficients, plots of the potential energy surfaces around minimal energy conical intersections, and movies of representative TBFs.

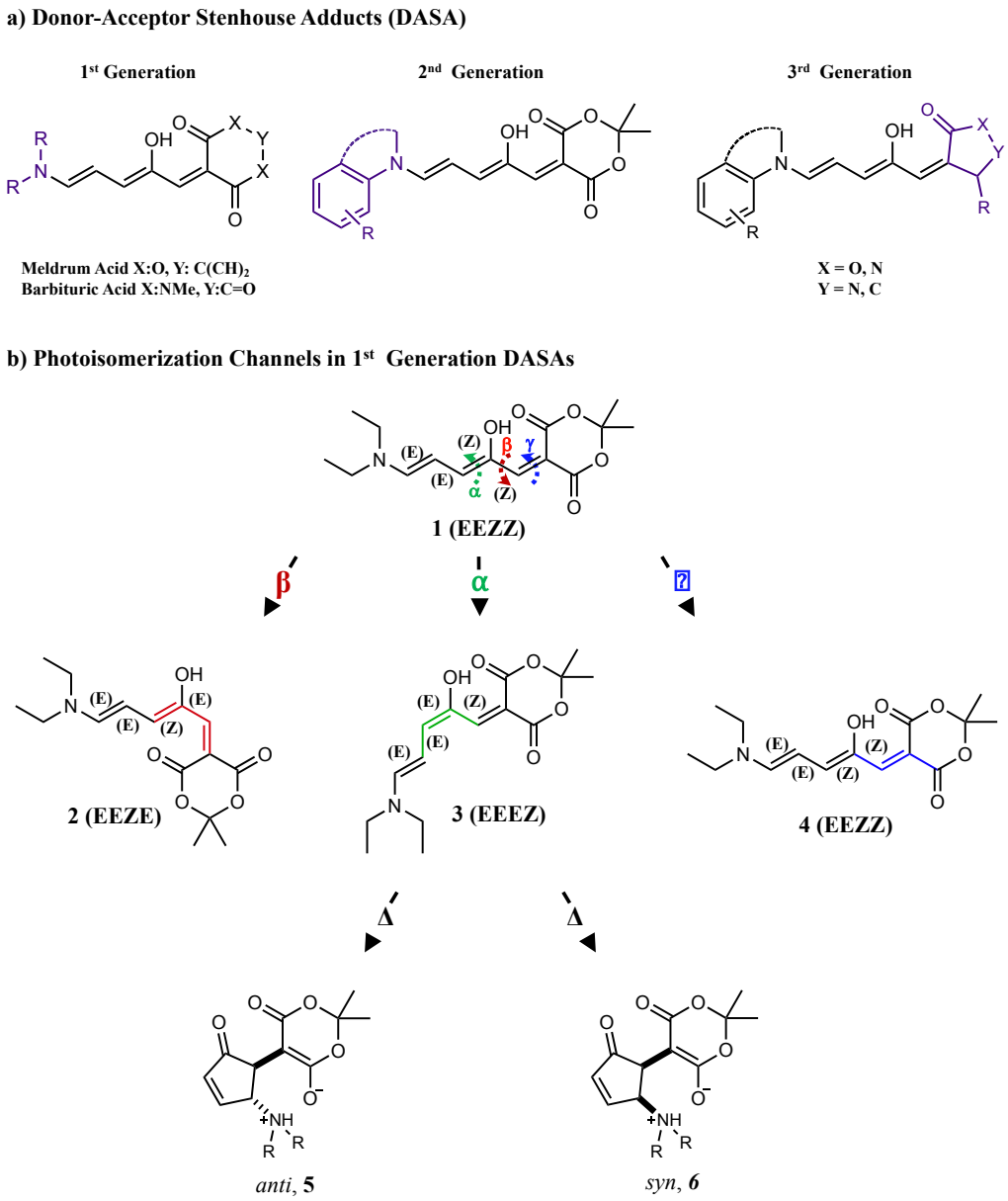

Figure 1. (**a**) DASA generations defined by their different donor and acceptor groups. (**b**) DASA in the ring-open form (**1**) undergoes a **Z**/**E** photoisomerization upon irradiation with 545nm light. Twisting around any of the C-C bonds along the hexatriene bridge leads to a conical intersection where the angle is approximately 90° (See Figure S1). Isomerization though α is followed by a thermal 4π-electrocyclization to form the *anti* (**5**) or *syn* (**6**) conformers of the ring-closed cyclopentenone form. The *anti* conformer is the only adduct that has been experimentally observed.

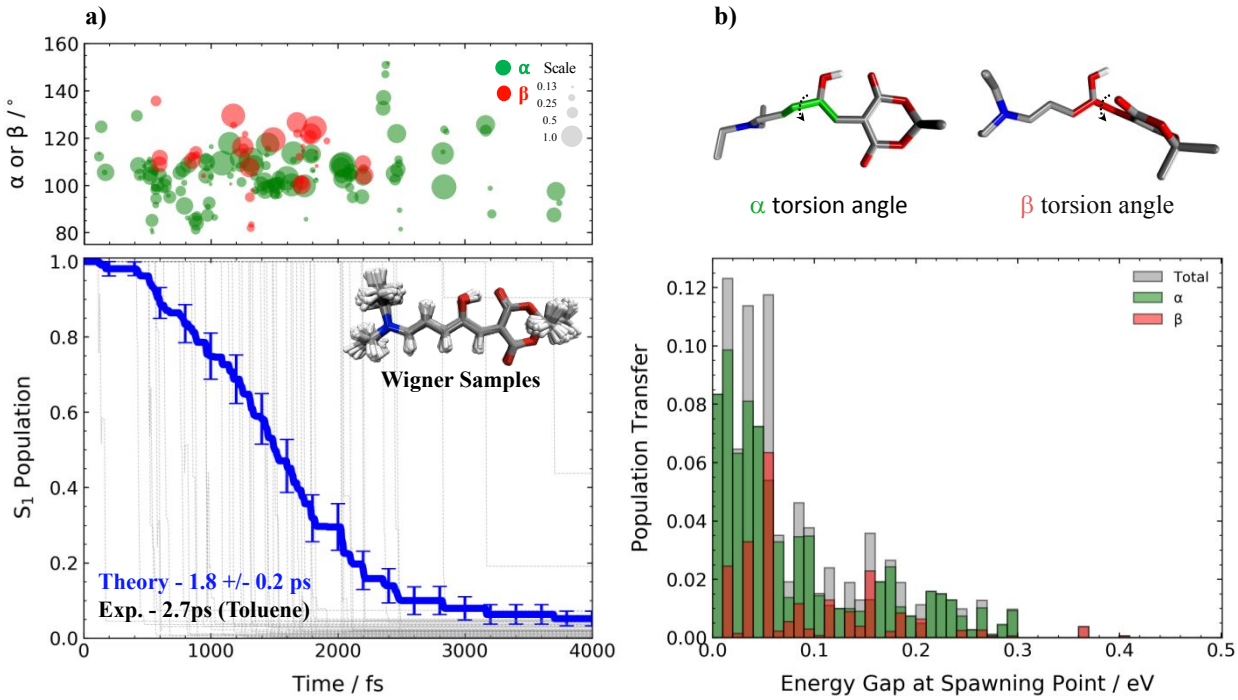

Figure 2. (**a**) (top) The spawning time vs the α (green) and β (red) dihedral angles at the spawning geometries from the AIMS trajectories. The spawning geometries are classified as α or β according to the twisting around the α and β dihedral angles (α ~ 90° for α and β ~ 90° for β). Since the potential energy surface is nearly symmetric with respect to the twisting direction (clockwise or counterclockwise), we report the absolute values of the α and β dihedral angles. This convention is used for all population transfer plots. The circle radius is proportional to the population transferred during the spawning event and separated into α and β channels. The population transfer is defined as the total population transferred to a child TBF from the beginning of coupled propagation until the child TBF becomes completely uncoupled (off-diagonal elements in the Hamiltonian become small). (bottom) The population of the wavepacket on the S_1 adiabat for the first 4ps of the photodynamics of Meldrum's acid 1st generation DASA. Error bars were obtained from bootstrap analysis of 236 TBFs from 50 initial conditions during the AIMS dynamics. (**b**) **(**top**)** The α and β torsion angles in DASA. **(**bottom**)** Histogram of the population transfer vs the energy gap of all S_1/S_0 spawning geometries from the entire AIMS simulation.

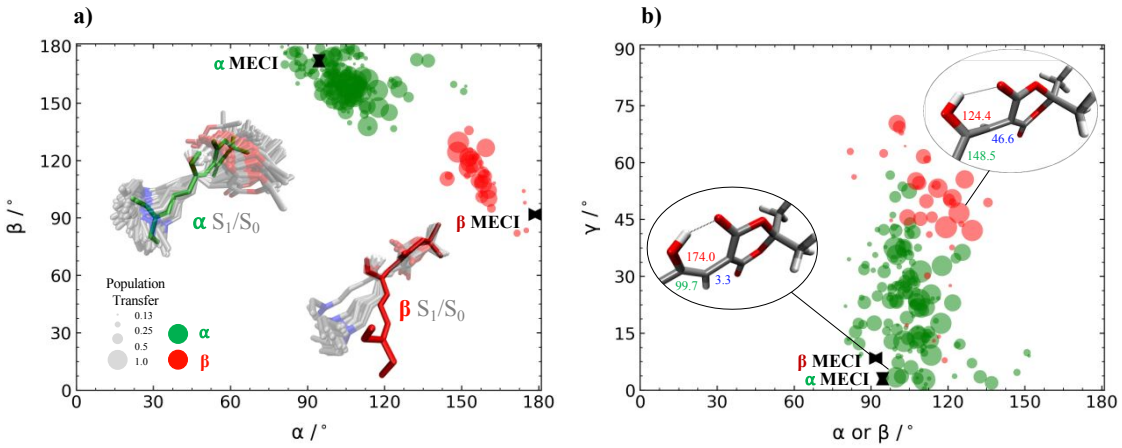

Figure 3. (**a**) The joint distribution between the α (green) and β (red) dihedral angles at the spawning geometries from the AIMS trajectories. Their MECI geometries (α-green and β-red) are overlaid with all spawning geometries from AIMS for comparison. **(b)** The joint distribution between α, β, and γ dihedral angles at the spawning geometries from the AIMS trajectories. Representative geometries are shown alongside their point. In both figures, the α and β dihedral angles for the MECI geometries are shown as black cones. The circle radius is proportional to the population transferred during the spawning event and separated into α and β channels.

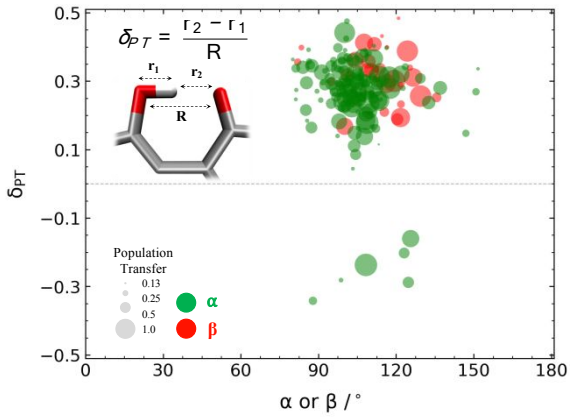

Figure 4. The proton transfer coordinate vs the α (green) and β (red) dihedral angles at the spawning geometries from the AIMS trajectories. The circle radius is proportional to the population transferred during the spawning event and separated into α and β channels. The proton transfer coordinate is defined in the inset.

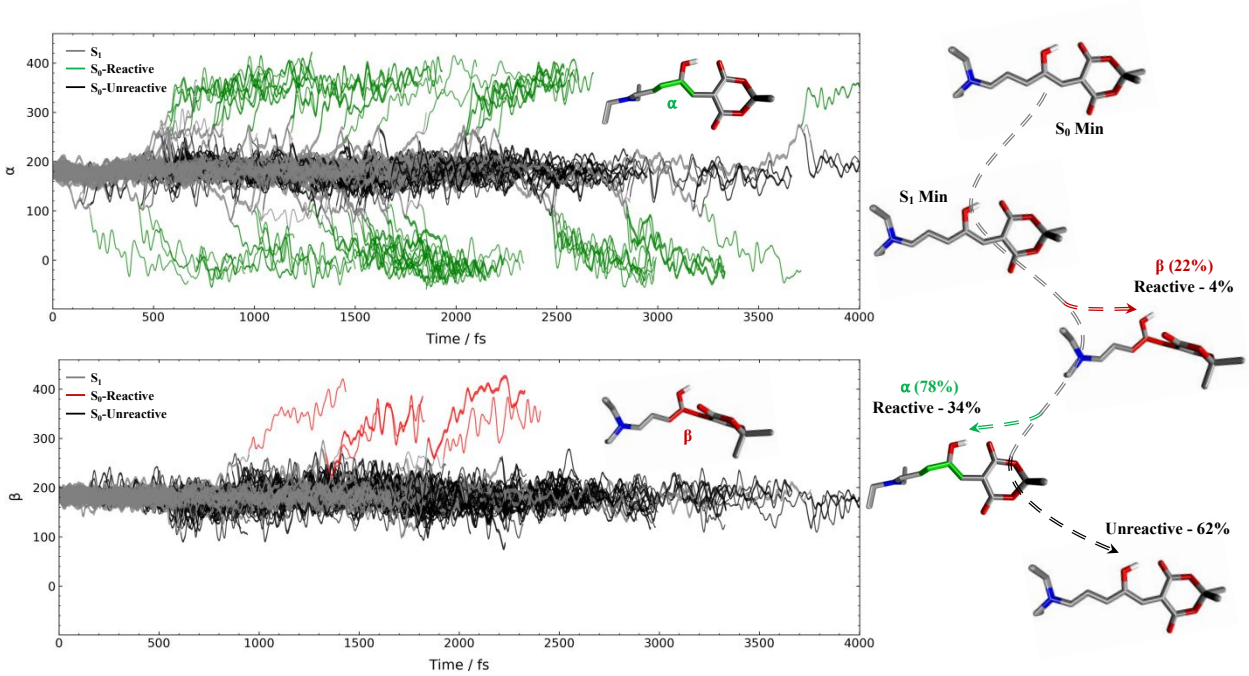

Figure 5. The time-evolution of the dihedral angles α and β through the course of the AIMS dynamics from all 50 initial conditions (236 TBFs). TBFs on S_1 are colored grey, while green (upper panel) and red (lower panel) lines represent "reactive" TBFs evolving from the photoreactant EEZZ on S_1 toward the α (EEEZ) or β (EEZE) photoproducts. All "unreactive" TBFs coming back to reform the photoreactant on S_0 are colored black. Reactive and unreactive pertains to those trajectories that did or did not form the cis photoproducts of α or β, respectively. The thickness of the line is proportional to the renormalized population at time t of a particular TBF during the AIMS dynamics. The branching ratio between α (green) and β(red) is shown along with the population of "reactive" and "unreactive" trajectories leading to the α (EEEZ) or β (EEZE) photoproducts.

References

1. White, T. J. *Photomechanical Materials, Composites, and Systems: Wireless Transduction of Light into Work*. Wiley: 2017.
2. Kim, T.; Zhu, L.; Al-Kaysi, R. O.; Bardeen, C. J. Organic Photomechanical Materials. *ChemPhysChem* **2014**, *15*, 400-414.
3. Tanchak, O. M.; Barrett, C. J. Light-Induced Reversible Volume Changes in Thin Films of Azo Polymers: The Photomechanical Effect. *Macromolecules* **2005**, *38*, 10566-10570.
4. Irie, M.; Kobatake, S.; Horichi, M. Reversible Surface Morphology Changes of a Photochromic Diarylethene Single Crystal by Photoirradiation. *Science* **2001**, *291*, 1769-1772.
5. Hugel, T.; Holland, N. B.; Cattani, A.; Moroder, L.; Seitz, M.; Gaub, H. E. Single-Molecule Optomechanical Cycle. *Science* **2002**, *296*, 1103-1106.
6. Yu, Y.; Nakano, M.; Ikeda, T. Photomechanics: Directed Bending of a Polymer Film by Light. *Nature* **2003**, *425*, 145.
7. Browne, W. R.; Feringa, B. L. Chiroptical Molecular Switches. *Mol. Switches* **2011**, *1*, 121-179.
8. Tian, H.; Yang, S. Recent Progresses on Diarylethene Based Photochromic Switches. *Chem. Soc. Rev.* **2004**, *33*, 85-97.
9. Irie, M.; Fukaminato, T.; Matsuda, K.; Kobatake, S. Photochromism of Diarylethene Molecules and Crystals: Memories, Switches, and Actuators. *Chem. Rev.* **2014**, *114*, 12174-12277.
10. Beharry, A. A.; Woolley, G. A. Azobenzene Photoswitches for Biomolecules. *Chem. Soc. Rev.* **2011**, *40*, 4422-4437.
11. Bleger, D.; Hecht, S. Visible-Light-Activated Molecular Switches. *Ang. Chem. Int. Ed.* **2015**, *54*, 11338-11349.
12. Pimienta, V.; Froute, C.; Deniel, M. H.; Lavabre, D.; Guglielmetti, R.; Micheau, J. C. Kinetic Modelling of the Photochromism and Photodegradation of a Spiro[Indoline-Naphthoxazine]. *J. Photochem. Photobio. A* **1999**, *122*, 199-204.
13. Li, X. L.; Li, J. L.; Wang, Y. M.; Matsuura, T.; Meng, J. B. Synthesis of Functionalized Spiropyran and Spirooxazine Derivatives and Their Photochromic Properties. *J. Photochem. Photobio. A* **2004**, *161*, 201-213.
14. Helmy, S.; Leibfarth, F. A.; Oh, S.; Poelma, J. E.; Hawker, C. J.; Read de Alaniz, J. Photoswitching Using Visible Light: A New Class of Organic Photochromic Molecules. *J. Amer. Chem. Soc.* **2014**, *136*, 8169-8172.
15. Helmy, S.; Oh, S.; Leibfarth, F. A.; Hawker, C. J.; Read de Alaniz, J. Design and Synthesis of Donor–Acceptor Stenhouse Adducts: A visible Light Photoswitch Derived from Furfural. *J. Org. Chem.* **2014**, *79*, 11316-11329.
16. Hemmer, J. R.; Poelma, S. O.; Treat, N.; Page, Z. A.; Dolinski, N. D.; Diaz, Y. J.; Tomlinson, W.; Clark, K. D.; Hooper, J. P.; Hawker, C.; Read de Alaniz, J. Tunable Visible and near Infrared Photoswitches. *J. Amer. Chem. Soc.* **2016**, *138*, 13960-13966.
17. Hemmer, J. R.; Page, Z. A.; Clark, K. D.; Stricker, F.; Dolinski, N. D.; Hawker, C. J.; Read de Alaniz, J. Controlling Dark Equilibria and Enhancing Donor–Acceptor Stenhouse Adduct Photoswitching Properties through Carbon Acid Design. *J. Amer. Chem. Soc.* **2018**, *140*, 10425-10429.

18. Lerch, M. M.; Wezenberg, S. J.; Szymanski, W.; Feringa, B. L. Unraveling the Photoswitching Mechanism in Donor–Acceptor Stenhouse Adducts. *J. Amer. Chem. Soc.* **2016**, *138*, 6344-6347.
19. Lerch, M. M.; Szymański, W.; Feringa, B. L. The (Photo) Chemistry of Stenhouse Photoswitches: Guiding Principles and System Design. *Chem. Soc. Rev.* **2018**, *47*, 1910-1937.
20. Lerch, M. M.; Di Donato, M.; Laurent, A. D.; Medved', M.; Iagatti, A.; Bussotti, L.; Lapini, A.; Buma, W. J.; Foggi, P.; Szymański, W. Solvent Effects on the Actinic Step of Donor–Acceptor Stenhouse Adduct Photoswitching. *Ang. Chem. Int. Ed.* **2018**, *57*, 8063-8068.
21. Lerch, M. M.; Medved′, M.; Lapini, A.; Laurent, A. D.; Iagatti, A.; Bussotti, L.; Szymanski, W.; Buma, W. J.; Foggi, P.; Di Donato, M. Tailoring Photoisomerization Pathways in Donor–Acceptor Stenhouse Adducts: The Role of the Hydroxy Group. *J. Phys. Chem. A* **2018**, *122*, 955-964.
22. Zulfikri, H.; Koenis, M. A. J.; Lerch, M. M.; Di Donato, M.; Szymański, W.; Filippi, C.; Feringa, B. L.; Buma, W. J. Taming the Complexity of Donor–Acceptor Stenhouse Adducts: Infrared Motion Pictures of the Complete Switching Pathway. *J. Amer. Chem. Soc.* **2019**, *141*, 7376-7384.
23. Di Donato, M.; Lerch, M. M.; Lapini, A.; Laurent, A. D.; Iagatti, A.; Bussotti, L.; Ihrig, S. P.; Medved', M.; Jacquemin, D.; Szymański, W.; Buma, W. J.; Foggi, P.; Feringa, B. L. Shedding Light on the Photoisomerization Pathway of Donor–Acceptor Stenhouse Adducts. *J. Amer. Chem. Soc.* **2017**, *139*, 15596-15599.
24. Lui, B. F.; Tierce, N. T.; Tong, F.; Sroda, M. M.; Lu, H.; Read de Alaniz, J.; Bardeen, C. J. Unusual Concentration Dependence of the Photoisomerization Reaction in Donor–Acceptor Stenhouse Adducts. *Photochem. Photobio. Sci.* **2019**, *18*, 1587-1595.
25. García-Iriepa, C.; Marazzi, M. Level of Theory and Solvent Effects on Dasa Absorption Properties Prediction: Comparing Td-Dft, Caspt2 and Nevpt2. *Materials* **2017**, *10*, 1025.
26. Laurent, A. D.; Medved', M.; Jacquemin, D. Using Time-Dependent Density Functional Theory to Probe the Nature of Donor–Acceptor Stenhouse Adduct Photochromes. *ChemPhysChem* **2016**, *17*, 1846-1851.
27. García-Iriepa, C.; Marazzi, M.; Sampedro, D. From Light Absorption to Cyclization: Structure and Solvent Effects in Donor-Acceptor Stenhouse Adducts. *ChemPhotoChem* **2019**, *0*.
28. Bull, J. N.; Carrascosa, E.; Mallo, N.; Scholz, M. S.; da Silva, G.; Beves, J. E.; Bieske, E. J. Photoswitching an Isolated Donor–Acceptor Stenhouse Adduct. *J. Phys. Chem. Lett.* **2018**, *9*, 665-671.
29. Hohenstein, E. G.; Luehr, N.; Ufimtsev, I. S.; Martinez, T. J. An Atomic Orbital-Based Formulation of the Complete Active Space Self-Consistent Field Method on Graphical Processing Units. *J. Chem. Phys.* **2015**, *142*, 224103.
30. Snyder, J. W.; Curchod, B. F. E.; Martínez, T. J. Gpu-Accelerated State-Averaged Complete Active Space Self-Consistent Field Interfaced with Ab Initio Multiple Spawning Unravels the Photodynamics of Provitamin D3. *J. Phys. Chem. Lett.* **2016**, *7*, 2444-2449.
31. Snyder, J. W., Jr.; Fales, B. S.; Hohenstein, E. G.; Levine, B. G.; Martinez, T. J. A Direct-Compatible Formulation of the Coupled Perturbed Complete Active Space Self-Consistent Field Equations on Graphical Processing Units. *J. Chem. Phys.* **2017**, *146*, 174113.
32. Ufimtsev, I. S.; Martínez, T. J. Quantum Chemistry on Graphical Processing Units. 1. Strategies for Two-Electron Integral Evaluation. *J. Chem. Theo. Comp.* **2008**, *4*, 222-231.
33. Ufimtsev, I. S.; Martinez, T. J. Quantum Chemistry on Graphical Processing Units. 2. Direct Self-Consistent-Field Implementation. *J. Chem. Theo. Comp.* **2009**, *5*, 1004-1015.

34. Ufimtsev, I. S.; Martinez, T. J. Quantum Chemistry on Graphical Processing Units. 3. Analytical Energy Gradients, Geometry Optimization, and First Principles Molecular Dynamics. *J. Chem. Theo. Comp.* **2009**, *5*, 2619-2628.
35. Ben-Nun, M.; Martínez, T. J. Nonadiabatic Molecular Dynamics: Validation of the Multiple Spawning Method for a Multidimensional Problem. *J. Chem. Phys.* **1998**, *108*, 7244-7257.
36. Ben-Nun, M.; Quenneville, J.; Martínez, T. J. Ab Initio Multiple Spawning: Photochemistry from First Principles Quantum Molecular Dynamics. *J. Phys. Chem. A* **2000**, *104*, 5161-5175.
37. Ben-Nun, M.; Martínez, T. J. Ab Initio Quantum Molecular Dynamics. *Adv. Chem. Phys.* **2002**, *121*, 439-512.
38. Yang, S.; Martínez, T. J. *Ab Initio Multiple Spawning: First Principles Dynamics around Conical Intersections*. World Scientific: Singapore: 2011; Vol. 17.
39. Liu, L.; Liu, J.; Martinez, T. J. Dynamical Correlation Effects on Photoisomerization: Ab Initio Multiple Spawning Dynamics with Ms-Caspt2 for a Model Trans-Protonated Schiff Base. *J. Phys. Chem. B* **2016**, *120*, 1940-1949.
40. Yu, J. K.; Liang, R.; Liu, F.; Martínez, T. J. First-Principles Characterization of the Elusive I Fluorescent State and the Structural Evolution of Retinal Protonated Schiff Base in Bacteriorhodopsin. *J. Amer. Chem. Soc.* **2019**, *141*, 18193-18203.
41. Liang, R.; Liu, F.; Martínez, T. J. Nonadiabatic Photodynamics of Retinal Protonated Schiff Base in Channelrhodopsin 2. *J. Phys. Chem. Lett.* **2019**, *10*, 2862-2868.
42. Shiozaki, T.; Győrffy, W.; Celani, P.; Werner, H.-J., Communication: Extended Multi-State Complete Active Space Second-Order Perturbation Theory: Energy and Nuclear Gradients. AIP: 2011.
43. Song, C.; Martínez, T. J. Reduced Scaling Extended Multi-State Caspt2 (Xms-Caspt2) Using Supporting Subspaces and Tensor Hyper-Contraction. *J. Chem. Phys.* **2020**, *152*, 234113.
44. Adamo, C.; Barone, V. Toward Reliable Density Functional Methods without Adjustable Parameters: The Pbe0 Model. *J. Chem. Phys.* **1999**, *110*, 6158-6170.
45. Coe, J. D.; Ong, M. T.; Levine, B. G.; Martínez, T. J. On the Extent and Connectivity of Conical Intersection Seams and the Effects of Three-State Intersections. *J. Phys. Chem. A* **2008**, *112*, 12559-12567.
46. Curchod, B. F. E.; Sisto, A.; Martínez, T. J. Ab Initio Multiple Spawning Photochemical Dynamics of Dmabn Using Gpus. *J. Phys. Chem. A* **2017**, *121*, 265-276.
47. Levine, B. G.; Martínez, T. J. Isomerization through Conical Intersections. *Ann. Rev. Phys. Chem.* **2007**, *58*, 613-634.